

Impact of charge transfer excitons on unidirectional exciton transport in lateral TMD heterostructures

Roberto Rosati,^{1,*} Sai Shradha,² Julian Picker,^{3,4} Andrey Turchanin,^{3,4} Bernhard Urbaszek,² and Ermin Malic¹

¹*Department of Physics, Philipps-Universität Marburg, Renthof 7, D-35032 Marburg, Germany*

²*Institute of Condensed Matter Physics, Technische Universität Darmstadt, 64289 Darmstadt, Germany*

³*Institute of Physical Chemistry, Friedrich Schiller University Jena, 07743 Jena, Germany*

⁴*Abbe Centre of Photonics, 07745 Jena, Germany*

Lateral heterostructures built of monolayers of transition metal dichalcogenides (TMDs) are characterized by a thin 1D interface exhibiting a large energy offset. Recently, the formation of spatially separated charge-transfer (CT) excitons at the interface has been demonstrated. The technologically important exciton propagation across the interface and the impact of CT excitons has remained in the dark so far. In this work, we microscopically investigate the spatiotemporal exciton dynamics in the exemplary hBN-encapsulated WSe₂-MoSe₂ lateral heterostructure and reveal a highly interesting interplay of energy offset-driven unidirectional exciton drift across the interface and efficient capture into energetically lower CT excitons at the interface. This interplay triggers a counterintuitive thermal control of exciton transport with a less efficient propagation at lower temperatures - opposite to the behavior in conventional semiconductors. We predict clear signatures of this intriguing exciton propagation both in far- and near-field photoluminescence experiments. Our results present an important step toward a microscopic understanding of the technologically relevant unidirectional exciton transport in lateral heterostructures.

Introduction - Monolayers of transition metal dichalcogenides (TMDs) can be grown side-by-side to form lateral heterostructures (Fig. 1) [1–4]. They typically exhibit a band offset at the interface, facilitating the formation of spatially separated charge-transfer (CT) excitons [5–8]. The latter have been experimentally demonstrated [6, 7], thanks to the recent developments in CVD growth techniques [3, 6, 9–12], allowing narrow interface widths comparable to the exciton Bohr radius. First studies on exciton and photo-carrier transport in lateral heterostructures have been performed [7, 10, 13–18]. Furthermore, in near-field spectroscopy narrow exciton distributions have been realized allowing the observation of an unidirectional exciton drift across the interface in a WSe₂-MoSe₂ lateral heterostructure [10, 13].

Excitons are neutral quasiparticles and their directional transport is challenging and has so far been mainly controlled in TMD monolayers or vertical TMD heterostructures, through strain profiles [19] or electric field [20]. In contrast, in lateral heterostructures, directional exciton transport occurs naturally due to the internal energy offset (Fig. 1) between the bands of the constituent materials. However, the role of CT excitons on the transport behaviour has been neglected so far, although they

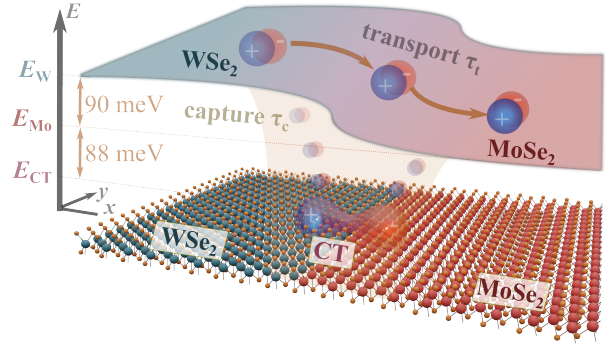


FIG. 1. Sketch of a lateral TMD heterostructure (bottom) and the resulting spatially varying excitonic energy landscape (top). Exciton propagation is governed by the interplay of the unidirectional transport across the interface (driven by the energy offset $E_W - E_{Mo}$) and the capture into the energetically lowest CT excitons X_{CT} .

are expected to play a crucial role when excitons propagate across the interface.

In this work, we microscopically model the spatiotemporal exciton dynamics in lateral TMD heterostructures focusing, in particular, on the exemplary hBN-encapsulated WSe₂-MoSe₂ structure. We reveal an intriguing interplay between the energy offset-driven unidirectional exciton propagation across the interface and the capture into the

* roberto.rosati@physik.uni-marburg.de

energetically lowest CT excitons at the interface. This results in an unexpected temperature dependence with a more pronounced exciton propagation at higher temperatures - contrary to the behaviour in conventional semiconductors. We predict distinct signatures of this intriguing propagation behaviour in near-field spectroscopy experiments, as the crossing point in space of the PL intensity of MoSe₂ and WSe₂ exciton transitions is not at the lateral crystal junction but a distance Δx several hundred nm away from it - in an excellent agreement with experimental data. Overall, our microscopic and material-specific approach sheds light on exciton propagation across the interface of technologically promising lateral TMD heterostructures, in particular emphasizing the importance of CT excitons.

Microscopic Model - We first microscopically calculate the exciton energy landscape in the hBN-encapsulated WSe₂-MoSe₂ lateral heterostructure by numerically solving the Schrödinger equation. We consider an interface width of 2.4 nm as realized in recent CVD-grown samples [6] and include the Coulomb interaction via a Keldysh-Rytova potential [21, 22]. We make use of the large difference between relative and total exciton mass [23] to separate the Schrödinger equation into two coupled equations (cf. the SI) [5, 6]. The first is a Wannier-like equation in the relative electron-hole position, determining if electrons and holes are bound. The solution enters the second equation, which provides an additional quantization in the center-of-mass position [5, 6]. This leads to the formation of CT excitons at the interface. They exhibit an energy E_{CT} that is clearly lower than the energy of MoSe₂ and WSe₂ excitons E_{Mo} and E_W , cf. Fig. 1. The considered heterostructure has a spatial energy offset $E_W - E_{Mo} = 90$ meV [10] at the interface and CT excitons are found to be 88 meV below E_{Mo} [6]. This energy offset is expected to drive the transport of excitons from the WSe₂ side toward the energetically favorable MoSe₂ side. While excitons are crossing the interface they are likely to be trapped into the energetically lower CT exciton states (Fig. 1).

Along the interface there is no energy offset, resulting in a drift-less diffusion [7, 24], while the offset-driven propagation across the interface can be described via one-dimensional Wigner functions $f_\alpha(x, q_x, t) = 1/L_y \int \sum_{q_y} \sum_{\mathbf{q}'} \langle \hat{X}_{\alpha, \mathbf{q}+\mathbf{q}'/2}^\dagger \hat{X}_{\alpha, \mathbf{q}-\mathbf{q}'/2} \rangle e^{i\mathbf{q}' \cdot \mathbf{r}} dy$. Here, x and q_x are the components across the interface (which is set to be along the y direction) of the center-of-mass position $\mathbf{r} = (x, y)$ and momen-

tum $\mathbf{q} = (q_x, q_y)$, while $L_{x,y}$ is the system length across/along the interface. The index $\alpha = W, Mo$ refers to excitons at the WSe₂ and the MoSe₂ side of the heterostructure, respectively, while $\hat{X}_{\alpha, \mathbf{q}}^{(\dagger)}$ are exciton annihilation (creation) operators [25, 26]. Using the Heisenberg equation of motion, we derive the spatiotemporal dynamics of the Wigner function yielding

$$\dot{f}_\alpha = -v_{q_x} \frac{\partial}{\partial x} f_\alpha + \frac{f_\alpha^\circ - f_\alpha}{\tau_p} + \dot{f}_\alpha^d + \dot{f}_\alpha^{cap}. \quad (1)$$

The first term describes the regular exciton propagation driven by the group velocity $v_{q_x} = \hbar q_x / M$ (with the exciton mass M) and the gradient in the occupation. The second term describes the phonon-driven thermalization toward the local Boltzmann distribution f_α° . This is modeled with a relaxation-time approximation with the microscopically obtained phonon-driven scattering rate τ_p [27]. As initial exciton occupation, we choose a Gaussian distribution centered at the interface or varied along the heterostructure (cf. the SI for more details).

While the first two contributions are also present in regular TMD monolayers, the third and the fourth term in Eq. (1) are specific to lateral TMD heterostructures. The third term describes the drift of excitons driven by the energy offset at the interface and reads

$$\dot{f}_\alpha^d(x, q_x, t) = \sum_{q'_x} \mathcal{V}(x, q_x - q'_x) f_\alpha(x, q'_x, t). \quad (2)$$

The spatial variation of exciton energies $E_\alpha(x)$ induces the superpotential $\mathcal{V}(x, q_x) = -\frac{i}{\hbar L_x} \int_{-x_V}^{x_V} dx' \left(E_\alpha(x + \frac{x'}{2}) - E_\alpha(x - \frac{x'}{2}) \right) e^{-iq_x x'}$, which corresponds to the regular semiclassical drift $1/\hbar \partial_x E_\alpha(x) \partial_{q_x} f_\alpha$ for smooth spatial variations of E_α (cf. the SI) [28]. Finally, the capture of optically excited MoSe₂/WSe₂ excitons into the energetically lower lying CT exciton states during the propagation across the interface is described by the fourth term in Eq. (1) reading

$$\dot{f}_\alpha^{cap} = \frac{\Delta n_\alpha f_\alpha^\circ - f_\alpha}{\tau_c}. \quad (3)$$

Here, we have introduced $\Delta n_\alpha = \frac{n_\alpha^\circ(x, t)}{n_\alpha(x, t)}$ as the ratio between the spatiotemporal exciton density $n_\alpha(x, t) = 1/L_x \sum_{q_x} f_\alpha(x, q_x, t)$ and its thermalized analogous $n_\alpha^\circ(x, t)$ after introduction of CT excitons. The capture process is driven by the emission of optical phonons [29, 30] with microscopically calculated scattering times τ_c [27]. The consequence is a decrease of WSe₂ and MoSe₂ exciton density n_α and

the build-up of a CT exciton density $n_{CT}(x, t)$ at the interface. Note that the capture is strongly temperature dependent via the local thermalized exciton density n_{α}° . At higher temperatures, the efficiency of the capture process is reduced, as excitons can escape by absorption of phonons [30].

The knowledge of exciton densities allows us to microscopically model the spatially and temporally resolved photoluminescence (PL), which is determined by a product of the exciton density and the oscillator strength of the involved exciton species. The PL intensity is described by an Elliot formula [31, 32], which we have generalized to include CT excitons [6]

$$I(E, x, t) = \sum_{\alpha} \frac{f_{\alpha}^{\circ}(x, \mathbf{q} = 0, t) \tilde{\gamma}_{\alpha} (\tilde{\gamma}_{\alpha} + \Gamma)}{(E - E_{\alpha})^2 + (\tilde{\gamma}_{\alpha} + \Gamma)^2} \quad (4)$$

with the exciton index $\alpha = W, Mo$ and CT and f_{α}° as the corresponding equilibrium exciton distribution. Furthermore, the PL is influenced by the temperature-dependent exciton-phonon scattering rate $\Gamma = \hbar/2\tau_p$ and the radiative decay rate $\tilde{\gamma} = \gamma_{\alpha} |\psi_{\alpha, \mathbf{q}=0}|^2$. Here γ_{α} is the oscillator strength, which is proportional to the probability of finding electrons and holes in the same position. This is about 35 smaller for spatially separated CT excitons compared to regular MoSe₂ and WSe₂ excitons [6], with the dipole furthermore having influence on the binding energy in analogy to the case of interlayer excitons [6, 33]. The momentum conservation implies that only the $\mathbf{q} = 0$ component of the exciton wavefunction $\psi_{\alpha, \mathbf{q}}$ allows radiative recombination.

Spatiotemporal exciton dynamics - In TMD monolayers, localized exciton densities propagate in space preserving their shape, which at low excitations only becomes spatially broader due to diffusion [34]. Exciton drift can be obtained by strain engineering [19, 35–40] or by applying electric fields in the case of vertical TMD heterostructures, where dipolar interlayer excitons are involved [20, 41, 42]. In lateral TMD heterostructures, the transport behavior is drastically different with qualitative changes in the shape of the propagating exciton densities as a result of an intriguing interplay of an energy offset-driven unidirectional exciton transport across the interface and capture into energetically lower CT excitons at the interface.

We investigate the exciton transport in hBN-encapsulated WSe₂-MoSe₂ lateral heterostructures by numerically evaluating Eq. (1), which explicitly takes into account the interplay of drift and cap-

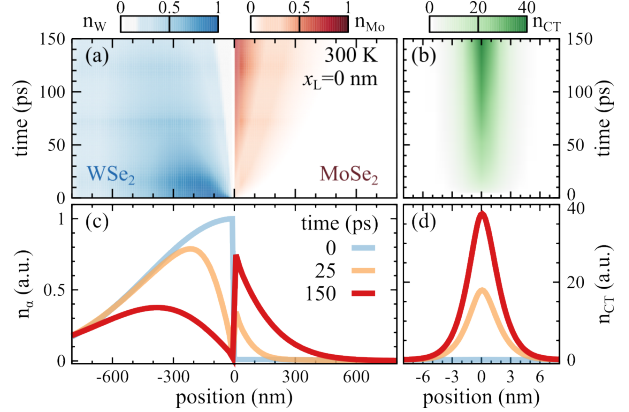


FIG. 2. Space-resolved densities of (a) WSe₂ and MoSe₂ excitons as well as of (b) CT excitons at 300 K after an optical excitation at the interface resonant with E_W . (c)-(d) 2D cuts of exciton densities at given times. The large CT exciton occupation and the exciton accumulation at the MoSe₂ side of the interface can be traced back to the interplay between unidirectional exciton drift across the interface and capture into CT excitons.

ture processes. Figure 2 shows the spatially and temporally resolved densities of (a, c) MoSe₂ and WSe₂ excitons as well as of (b, d) CT excitons after an optical excitation at the interface (laser position at $x_L = 0$ nm) with a typical diffraction-limited spot (FWHM of 1 μm). The excitation is set to be resonant to the WSe₂ exciton and creates an initially broad spatial exciton density n_W at the WSe₂ side of the lateral heterostructure, with a small off-resonant occupation of MoSe₂ excitons (about 100 times smaller than for WSe₂) [43, 44], cf. the blue line in Fig. 2(c). This changes rapidly, as the energy offset $E_W - E_{Mo} = 90$ meV at the interface gives rise to a drift of excitons toward the energetically more favorable MoSe₂ side (Fig. 1). This unidirectional transport leads to an accumulation of exciton density at the MoSe₂ side of the interface, cf. the red line in Fig. 2(c). The exciton accumulation becomes visible after few tens of picoseconds and it extends over hundreds of nanometers into the MoSe₂ side. Such broad spatial extensions are already observable in experimental setups with a spatial resolution of a few hundreds of nanometers [7, 10, 19, 34, 45, 46].

During the unidirectional propagation across the interface, excitons can become trapped into the energetically lower-lying CT excitons. This results in a local depletion of the the exciton density n_W at the interface, cf. the orange and red line in Fig. 2(c). At the same time the density of CT excitons considerably increases (Figs. 2(b,d)). Its maximum

becomes almost two orders of magnitude larger than the excited density within the first 150 ps. The efficient trapping into CT excitons has important fundamental and technological applications. Since CT excitons are dipolar and repel each other, the quick increase of their density can explain the recently observed nonlinear, dipole-driven CT-exciton diffusion along the interface [7]. Since CT excitons have a small binding energy of few tens of meV [6], the trapping of WSe₂ or MoSe₂ excitons could lead to their efficient dissociation, which is favorable for many optoelectronic devices.

In a nutshell, the drift-induced unidirectional propagation results in an exciton accumulation at the low-energy side of the interface and the efficient capture processes give rise to large CT exciton densities. The formation time and the height of exciton accumulations are determined by the interplay of exciton capture and drift and their competition can be thermally controlled.

Temperature control of exciton propagation - Carrier drift becomes generally faster at lower temperatures as here the efficiency of scattering with phonons is decreased. Interestingly, we find the opposite behavior for exciton propagation in lateral TMD heterostructures. Figure 3(a) illustrates the temperature-dependent spatiotemporal dynamics of MoSe₂ and WSe₂ excitons. The height of the drift-induced exciton accumulation at the MoSe₂ side becomes surprisingly smaller with decreasing temperature T , i.e. the unidirectional transport becomes weaker at lower T . This behavior can be traced back to the efficient trapping process into CT excitons at the interface. It suppresses the drift by capturing the propagating WSe₂ excitons before they reach the MoSe₂ side. To show this, we consider the case without CT excitons (corresponding to lateral heterostructures with larger interface widths [6]). Here, we find the expected temperature trend, i.e. a faster propagation toward the low-energy side at smaller temperatures, cf. Fig. 3(b). Note that the accumulation is overall one order of magnitude higher without CT excitons. The larger impact of the capture at smaller temperatures is due to a suppression of the counteracting escape processes driven by phonon absorption.

The exciton accumulation at the MoSe₂ side after a resonant excitation of WSe₂ excitons is a hallmark for the unidirectional exciton transport. This can be revealed in space-integrated and time-resolved PL, cf. Fig. 3(c). The spectrum initially shows only one peak X_W stemming from optically excited WSe₂ excitons centered at E_W . The energy offset-

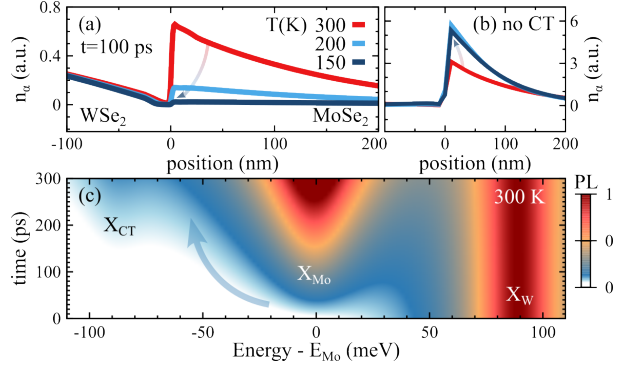


FIG. 3. (a) Temperature-dependent accumulation of exciton density after 100 ps. The decrease as a function of temperature is opposite to the behaviour in conventional semiconductors, which we obtain when (b) CT excitons are switched off. (c) Space-integrated and time-resolved PL spectrum (normalized to the intensity of X_W), with a delayed formation of the X_{Mo} resonance. The latter is due to the energy offset-driven propagation across the interface.

induced exciton drift results in the formation of an additional resonance at E_{Mo} after a certain time delay. While the linewidth of this peak is fixed by radiative-recombination and phonon-mediated scattering [27], its height relative to X_W increases in time due to the unidirectional exciton propagation. At room temperature, X_{Mo} becomes as intense as X_W after approximately 200 ps. The situation is drastically different at smaller temperatures, where the capture-induced suppression of exciton propagation results in a negligible intensity of the drift-driven X_{Mo} resonance (cf. the SI). Note that an excitation resonant to E_{Mo} does not result in the formation of a X_W peak, as excitons would need to increase their energy by about 90 meV. This indicates the possibility of an optical control of the unidirectional exciton drift that is potentially interesting for excitonic diodes [10, 47].

Surprisingly, we also observe the appearance of a small CT exciton peak X_{CT} after few hundreds of picoseconds even at room temperature (Fig. 3(c)). The peak becomes more intense at reduced temperatures in particular compared to the X_{Mo} resonance. The formation time of the CT exciton resonance is, however, close to typical PL decay times of 150-200 ps in WSe₂-MoSe₂ lateral heterostructures [9, 10]. As a consequence, such a small CT exciton peak present in time-resolved PL spectra might be difficult to observe in time-integrated, energy-resolved far-field PL. Thus, we investigate now optical excitation in the nanometer range as

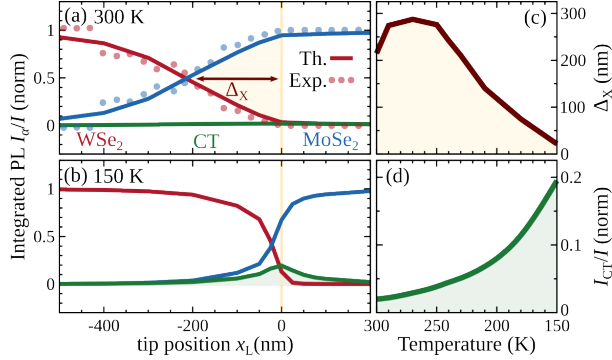


FIG. 4. Intensity of the X_{Mo} , X_W and X_{CT} resonances in PL spectra at (a) 300 K and (b) 150 K after a near-field excitation at different laser positions (normalized to the total intensity I). The vertical yellow line indicates the position of the interface. The dots show the corresponding experimental measurement taken from Ref. [10]. The interplay of the energy offset-driven unidirectional exciton propagation and capture into CT excitons breaks the symmetry resulting in a spatial offset Δ_X from the interface, at which the emission from WSe_2 and $MoSe_2$ excitons is equal - in excellent agreement between theory and experiment. (c)-(d) Temperature-dependent offset Δ_X and CT exciton emission I_{CT}/I .

can be realized in near-field spectroscopy.

Near-field photoluminescence - In near-field scanning microscopy, we focus on excitation spots with FWHM of 50 nm and varying position in space. In this way, we create asymmetric $MoSe_2$ and WSe_2 exciton occupations as realized in recent experiments [10, 13, 48]. Figure 4(a) shows the relative space- and time-integrated PL intensity as a function of the laser position across the interface. We consider an exciton decay time of 175 ps as extracted from measurements on the same lateral heterostructure [10]. When exciting at the $MoSe_2$ side, the PL is, as expected, clearly dominated by I_{Mo} and the I_W signal is negligible, cf. the blue and red line in Fig. 4(a).

Naively, we would expect excitations on the WSe_2 side to induce PL dominated by the X_W resonance. The predicted PL is, however, drastically different due to energy offset-driven unidirectional transport to the $MoSe_2$ side and the capture processes into CT excitons at the interface. When the excitation spot is far away from the interface (>500 nm), the PL behaves as expected and I_W dominates. However, for excitation closer to the interface (<200 nm), I_{Mo} becomes more pronounced than I_W . Note that this occurs for excitation spots with a distance 4

times larger than the excitation confinement of 50 nm. The reason for this behavior is the efficient exciton drift, which drives the excited WSe_2 excitons toward the energetically more favorable $MoSe_2$ side. The drift efficiency can be quantified by the spatial offset Δ_X from the interface with an equal PL intensity from $MoSe_2$ and WSe_2 excitons. Without a drift, we find Δ_X to be 0, as expected. At room temperature, we predict a value of $\Delta_X \approx 215$ nm. This is in excellent agreement with recent near-field experiments [10, 13], cf. the dots in Fig. 4(a).

Given the thermal control of exciton transport discussed above, we investigate the near-field PL at the lower temperature of 150 K (Fig. 4(b)). We observe that the spatial offset becomes smaller with $\Delta_X \approx 20$ nm reflecting the capture-induced suppression of the exciton drift at decreasing temperatures (cf. also Fig. 3(a)). This is confirmed by a temperature study in Fig. 4(c), where we interestingly also find a slight increase of Δ_X for temperatures from 300 to 280 K. This is induced by the competition between the intrinsic energy offset-driven exciton drift and exciton capture (both more efficient at smaller temperatures). The efficient capture is further demonstrated in the increasing PL intensity of CT excitons at lower temperatures, cf. Fig. 4(d). Here, the near-field excitation allows to visualize the CT resonance even in time-integrated PL.

Conclusions - Based on a microscopic, material specific and predictive approach, we have studied exciton transport in lateral TMD heterostructures. We demonstrate a pronounced unidirectional exciton drift due to the energy offset across the interface resulting in an accumulation of excitons at one side of the interface. Furthermore, we predict a crucial impact of capture processes into the energetically lower-lying charge transfer excitons at the interface. Finally, we demonstrate that temperature is the key knob to control the interplay between the unidirectional exciton drift and the capture-induced formation of charge transfer excitons. Based on the gained microscopic knowledge, we provide concrete recipes for detecting the intriguing exciton propagation both in far- and near-field photoluminescence experiments. Our findings have also a potential technological importance for devices based on unidirectional exciton transport in lateral heterostructures.

ACKNOWLEDGMENTS

We acknowledge support by the Deutsche Forschungsgemeinschaft (DFG) via SPP 2244 and CRC 1083 (project B9). We also thank Giuseppe Meneghini for graphical support in Fig. 1 and for discussions together with Jamie Fitzgerald.

-
- [1] X. Duan, C. Wang, J. C. Shaw, R. Cheng, Y. Chen, H. Li, X. Wu, Y. Tang, Q. Zhang, A. Pan, J. Jiang, R. Yu, Y. Huang, and X. Duan, *Nat. Nanotechnol.* **9**, 1024 (2014).
 - [2] C. Huang, S. Wu, A. M. Sanchez, J. J. P. Peters, R. Beanland, J. S. Ross, P. Rivera, W. Yao, D. H. Cobden, and X. Xu, *Nat. Mater.* **13**, 1096 (2014).
 - [3] S. Xie, L. Tu, Y. Han, L. Huang, K. Kang, K. U. Lao, P. Poddar, C. Park, D. A. Muller, R. A. DiStasio, and J. Park, *Science* **359**, 1131 (2018).
 - [4] P. K. Sahoo, S. Memaran, Y. Xin, L. Balicas, and H. R. Gutiérrez, *Nature* **553**, 63 (2018).
 - [5] K. W. Lau, Calvin, Z. Gong, H. Yu, and W. Yao, *Phys. Rev. B* **98**, 115427 (2018).
 - [6] R. Rosati, I. Paradisanos, L. Huang, Z. Gan, A. George, K. Watanabe, T. Taniguchi, L. Lombez, P. Renucci, A. Turchanin, B. Urbaszek, and E. Malic, *Nat. Commun.* **14**, 2438 (2023).
 - [7] L. Yuan, B. Zheng, Q. Zhao, R. Kempt, T. Brumme, A. B. Kuc, C. Ma, S. Deng, A. Pan, and L. Huang, *ACS Nano* **17**, 15379 (2023).
 - [8] M. V. Durnev and D. S. Smirnov, “Intervalley mixing of interface excitons at lateral heterojunctions,” (2024), arXiv:2408.10170 [cond-mat.mes-hall].
 - [9] E. Najafidehaghani, Z. Gan, A. George, T. Lehnert, G. Q. Ngo, C. Neumann, T. Bucher, I. Staudé, D. Kaiser, T. Vogl, U. Hübner, U. Kaiser, F. Eilenberger, and A. Turchanin, *Adv. Funct. Mater.* **31**, 2101086 (2021).
 - [10] D. Beret, I. Paradisanos, H. Lamsaadi, Z. Gan, E. Najafidehaghani, A. George, T. Lehnert, J. Biskupek, U. Kaiser, S. Shree, A. Estrada-Real, D. Lagarde, X. Marie, P. Renucci, K. Watanabe, T. Taniguchi, S. Weber, V. Paillard, L. Lombez, J.-M. Poumirol, A. Turchanin, and B. Urbaszek, *npj 2D Mater. Appl.* **6**, 84 (2022).
 - [11] M.-Y. Li, Y. Shi, C.-C. Cheng, L.-S. Lu, Y.-C. Lin, H.-L. Tang, M.-L. Tsai, C.-W. Chu, K.-H. Wei, J.-H. He, W.-H. Chang, K. Suenaga, and L.-J. Li, *Science* **349**, 524 (2015).
 - [12] N. Ichinose, T. Hotta, M. Maruyama, Z. Liu, R. Canton-Vitoria, S. Okada, F. Zeng, F. Zhang, T. Taniguchi, K. Watanabe, *et al.*, arXiv preprint arXiv:2208.12696 (2022).
 - [13] H. Lamsaadi, D. Beret, I. Paradisanos, P. Renucci, D. Lagarde, X. Marie, B. Urbaszek, Z. Gan, A. George, K. Watanabe, T. Taniguchi, A. Turchanin, L. Lombez, N. Combe, V. Paillard, and J.-M. Poumirol, *Nat. Commun.* **14**, 5881 (2023).
 - [14] M. Z. Bellus, M. Mahjouri-Samani, S. D. Lane, A. D. Oyedele, X. Li, A. A. Puzos, D. Geoeagan, K. Xiao, and H. Zhao, *ACS Nano* **12**, 7086 (2018).
 - [15] M. Shimasaki, T. Nishihara, K. Matsuda, T. Endo, Y. Takaguchi, Z. Liu, Y. Miyata, and Y. Miyauchi, *ACS Nano* (2022), 10.1021/acsnano.2c01890.
 - [16] B. Kundu, P. Mondal, D. Tebbe, M. N. Hasan, S. K. Chakraborty, M. Metzelaars, P. Kögerler, D. Karimakar, G. K. Pradhan, C. Stampfer, B. Beschoten, L. Waldecker, and P. K. Sahoo, *Nano Letters* **24**, 14615 (2024).
 - [17] Y. Zhong, S. Yue, H. Liu, Y. Xia, A. Pan, S. Chen, and X. Liu, “Ultrafast carriers’ separation imaging in WS₂-WSe₂ in plane heterojunction by transient reflectivity microscopy,” (2024), arXiv:2403.10848 [cond-mat.mes-hall].
 - [18] B. Kundu, P. Chakraborty, A. Dhara, R. Rosati, C. Samanta, S. K. Chakraborty, S. Sahoo, S. Dhara, S. P. Dash, E. Malic, S. Lodha, and P. K. Sahoo, “Trion engineered multimodal transistors in two dimensional bilayer semiconductor lateral heterostructures,” (2024), arXiv:2411.01257 [physics.app-ph].
 - [19] R. Rosati, R. Schmidt, S. Brem, R. Perea-Causín, I. Niehues, J. Kern, J. A. Preuß, R. Schneider, S. Michaelis de Vasconcellos, R. Bratschitsch, and E. Malic, *Nat. Commun.* **12**, 7221 (2021).
 - [20] D. Unuchek, A. Ciarrocchi, A. Avsar, K. Watanabe, T. Taniguchi, and A. Kis, *Nature* **560**, 340 (2018).
 - [21] L. Keldysh, *JETPL* **29**, 658 (1979).
 - [22] N. S. Rytova, *Proc. MSU, Phys., Astron.* **30**, 3 (1967).
 - [23] A. Kormányos, G. Burkard, M. Gmitra, J. Fabian, V. Zólyomi, N. D. Drummond, and V. Fal’ko, *2D Mater.* **2**, 022001 (2015).
 - [24] X. P. Vögele, D. Schuh, W. Wegscheider, J. P. Kotthaus, and A. W. Holleitner, *Phys. Rev. Lett.* **103**, 126402 (2009).
 - [25] R. Rosati, R. Perea-Causín, S. Brem, and E. Malic, *Nanoscale* **12**, 356 (2020).
 - [26] S. Brem, M. Selig, G. Berghäuser, and E. Malic, *Sci. Rep.* **8**, 8238 (2018).
 - [27] M. Selig, G. Berghäuser, A. Raja, P. Nagler, C. Schüller, T. F. Heinz, T. Korn, A. Chernikov,

- E. Malic, and A. Knorr, *Nat. Commun.* **7**, 13279 (2016).
- [28] O. Hess and T. Kuhn, *Phys. Rev. A* **54**, 3347 (1996).
- [29] M. Glanemann, V. M. Axt, and T. Kuhn, *Phys. Rev. B* **72**, 045354 (2005).
- [30] D. Reiter, M. Glanemann, V. M. Axt, and T. Kuhn, *Phys. Rev. B* **75**, 205327 (2007).
- [31] S. W. Koch, M. Kira, G. Khitrova, and H. M. Gibbs, *Nat. Mater.* **5**, 523 (2006).
- [32] S. Brem, A. Ekman, D. Christiansen, F. Katsch, M. Selig, C. Robert, X. Marie, B. Urbaszek, A. Knorr, and E. Malic, *Nano Lett.* **20**, 2849 (2020).
- [33] S. Latini, K. T. Winther, T. Olsen, and K. S. Thygesen, *Nano Lett.* **17**, 938 (2017).
- [34] M. Kulig, J. Zipfel, P. Nagler, S. Blanter, C. Schüller, T. Korn, N. Paradiso, M. M. Glazov, and A. Chernikov, *Phys. Rev. Lett.* **120**, 207401 (2018).
- [35] M. G. Harats, J. N. Kirchhof, M. Qiao, K. Greben, and K. I. Bolotin, *Nat. Photonics* **14**, 324 (2020).
- [36] D. F. Cordovilla Leon, Z. Li, S. W. Jang, C.-H. Cheng, and P. B. Deotare, *Appl. Phys. Lett.* **113**, 252101 (2018).
- [37] K. Datta, Z. Lyu, Z. Li, T. Taniguchi, K. Watanabe, and P. B. Deotare, *Nat. Photonics* **16**, 242 (2022).
- [38] H. Lee, Y. Koo, J. Choi, S. Kumar, H.-T. Lee, G. Ji, S. H. Choi, M. Kang, K. K. Kim, H.-R. Park, H. Choo, and K.-D. Park, *Sci. Adv.* **8**, eabm5236 (2022).
- [39] E. D. S. Nysten, M. Weiß, B. Mayer, T. M. Petzack, U. Wurstbauer, and H. J. Krenner, *Advanced Materials* **36**, 2402799 (2024).
- [40] A. M. Kumar, D. Yagodkin, R. Rosati, D. J. Bock, C. Schattauer, S. Tobisch, J. Hagel, B. Höfer, J. N. Kirchhof, P. Hernández López, K. Burfeindt, S. Heeg, C. Gahl, F. Libisch, E. Malic, and K. I. Bolotin, *Nat. Commun.* **15**, 7546 (2024).
- [41] F. Tagarelli, E. Lopriore, D. Erkensten, R. Perea-Causín, S. Brem, J. Hagel, Z. Sun, G. Pasquale, K. Watanabe, T. Taniguchi, E. Malic, and A. Kis, *Nat. Photonics* **17**, 615 (2023).
- [42] J. Hagel, S. Brem, and E. Malic, *2D Mater.* **10**, 014013 (2022).
- [43] S. Shree, M. Semina, C. Robert, B. Han, T. Amand, A. Balocchi, M. Manca, E. Courtade, X. Marie, T. Taniguchi, K. Watanabe, M. M. Glazov, and B. Urbaszek, *Phys. Rev. B* **98**, 035302 (2018).
- [44] C. M. Chow, H. Yu, A. M. Jones, J. R. Schaibley, M. Koehler, D. G. Mandrus, R. Merlin, W. Yao, and X. Xu, *npj 2D Mater. and App.* **1**, 33 (2017).
- [45] D. F. Cordovilla Leon, Z. Li, S. W. Jang, and P. B. Deotare, *Phys. Rev. B* **100**, 241401 (2019).
- [46] G. D. B. Vazquez, G. L. G. Morganti, A. Block, N. F. van Hulst, M. Liebel, and K.-J. Tielrooij, *Adv. Electron. Mater.* **10**, 2300584 (2024).
- [47] L. Butov, *Superlattices and Microstructures* **108**, 2 (2017), indirect Excitons: Physics and Applications.
- [48] A. Albagami, S. Ambardar, H. Hrim, P. K. Sahoo, Y. Emirov, H. R. Gutiérrez, and D. V. Voronine, *ACS Applied Materials & Interfaces* **14**, 11006 (2022).

Supplementary Information for Impact of charge transfer excitons on unidirectional exciton transport in lateral TMD heterostructures

Roberto Rosati,^{1,*} Sai Shradha,² Julian Picker,^{3,4} Andrey Turchanin,^{3,4} Bernhard Urbaszek,² and Ermin Malic¹

¹*Department of Physics, Philipps-Universität Marburg, Renthof 7, D-35032 Marburg, Germany*

²*Institute of Condensed Matter Physics, Technische Universität Darmstadt, 64289 Darmstadt, Germany*

³*Institute of Physical Chemistry, Friedrich Schiller University Jena, 07743 Jena, Germany*

⁴*Abbe Centre of Photonics, 07745 Jena, Germany*

1. EXCITON ENERGY LANDSCAPE

We investigate lateral heterostructures (LHs) based on transition metal dichalcogenide monolayers (TMD). We solve the Schrödinger equation including the space-dependent energy landscape due to the presence of an interface, cf. Fig. S1. The two different materials induce an in-plane variation of energy, which we describe via the single-particle band-edge energies $E_{c/v}^0(\mathbf{r}_{c/v})$ of conduction- and valence-band electrons, respectively, with $\mathbf{r}_{c/v}$ being their respective positions. These single-particle energies read $E_{c/v}^0(\mathbf{r}_{c/v}) = \Delta E_{c/v}(1 - \tanh(4x_{c/v}/w))/2 + E_{\text{Mo}}^0(1 \pm 1)/2$ with $+$ ($-$) for c (v), cf. Fig. S1(b) [1, 2]. Here, w denotes a finite width of the interface, reflecting the typical situation in real samples due to spontaneous alloying [3, 4]. In particular, we consider a narrow interface of $w=2.4$ nm, as recently realized experimentally [2]. While lateral heterostructures involving TMDs with different chalcogen atoms have a lattice mismatch, in WSe₂-MoSe₂ we can assume a strain-free interface [5, 6]. The conduction and valence bands form an offset $\Delta E_c, \Delta E_v$ at the interface, typically inducing a type-II alignment [7–11]. In the specific case of WSe₂-MoSe₂ LH, the conduction band minimum is located in the MoSe₂ layer [12], hence only the bright valley is relevant for charge transfer (CT) excitons in WSe₂-MoSe₂ [2]. We take a valence-band offset $\Delta E_v=215$ meV in agreement with the microscopic estimation in similar LHs [12]. In addition, the two materials exhibit also a different bandgap with $E_{\text{W}}^0 - E_{\text{Mo}}^0 = 90$ meV [13] leading to $\Delta E_c = \Delta E_v + 90$ meV. The different bandgap at the two sides of the heterostructure is different than in the case of gate-induced homojunctions [14–16], where the band offsets are the same ($\Delta E_c = \Delta E_v$) and where bound excitons confined to few tens of nanometers can appear [17, 18]. The type-II alignment allows for a continuum of unbound CT electron-hole pairs, with electrons and holes stemming from different sides of the interface and forming an unbound continuum with the minimum energy $E_{\text{CT}}^0 = E_{\text{Mo}}^0 - \Delta E_v = E_{\text{W}}^0 - \Delta E_c$ (cf. the purple oval in Fig. S1(b)).

To investigate if also bound CT excitons can form, we include the electron-hole Coulomb interaction $V_C(\mathbf{r}_r)$, which is described by a generalized Keldysh potential [19–21] for charges in a thin-film surrounded by a spatially-homogeneous dielectric environment [19–21]. Here we have introduced the center-of-mass and relative positions $\mathbf{r} \equiv (x, y)$ and \mathbf{r}_r , respectively. In view of the difference between the relative and total exciton mass μ and M , respectively, the resulting Schrödinger equation can be separated in equations for the relative and the center-of-mass motion [1, 2] yielding

$$\left[\frac{-\hbar^2 \nabla_{\mathbf{r}_r}^2}{2\mu} + V_C(\mathbf{r}_r) + V^x(\mathbf{r}_r) \right] \phi_j^x(\mathbf{r}_r) = \tilde{E}_j(x) \phi_j^x(\mathbf{r}_r), \quad (1a)$$

$$\left[-\frac{\hbar^2}{2M} \partial_x^2 + \tilde{E}_j(x) \right] \psi_{n,j}(x) = E_{n,j} \psi_{n,j}(x), \quad (1b)$$

where $V^x(\mathbf{r}_r) = E_c^0(\mathbf{r}_r, x) - E_v^0(\mathbf{r}_r, x)$ acts as an interface potential given by the space-dependent band edges $E_{c,v}^0$ and the masses μ and M , which we include as material-specific input parameters from first-principles calculations [22]. Here, Eq. (1a) is a Wannier-like equation stating if electrons and holes can bind together via a quantization in relative motion, with $j=1s, 2s, 3s, \dots$ labeling the bound states. In this work, we focus on the energetically lowest 1s excitons justified by the large energy separation of excited states. The eigenenergies $\tilde{E}_j(x)$ found by solving Eq. (1a) act as a potential in Eq. (1b), where they can induce an additional quantization in the center-of-mass position, resulting in the emergence of bound CT excitons localized at the interface. In the monolayer limit of no band offsets, i.e. $\Delta E_{c/v} = 0$, Eq. (1a) becomes the well-known Wannier equation with a space-independent potential and $\tilde{E}_j(x) \equiv \tilde{E}_j$.

*Electronic address: roberto.rosati@physik.uni-marburg.de

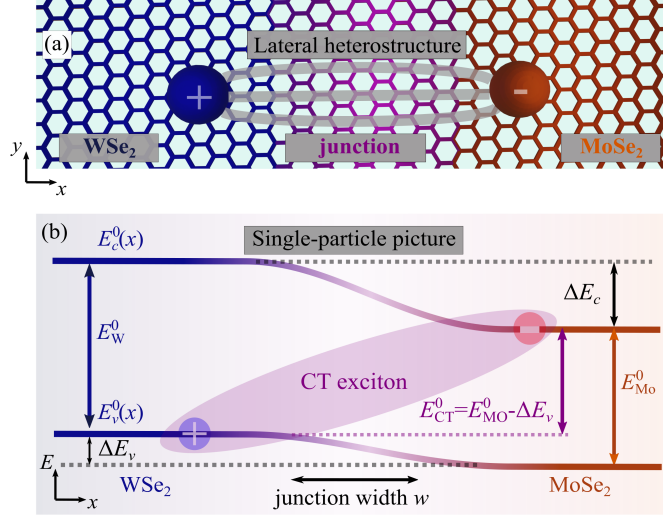


Fig. S1: (a) Sketch of a lateral WSe₂-MoSe₂ heterostructure. (b) The two materials have intrinsic bandgaps E_{Mo}^0 and E_{W}^0 and forming conduction and valence band offsets ΔE_c , ΔE_v around the junction. Spatially-separated electrons and holes across the interface form charge-transfer (CT) excitons with the corresponding continuum energy $E_{\text{CT}}^0 = E_{\text{Mo}}^0 - \Delta E_v$.

In this limit, the center-of-mass equation (Eq. (1b)) becomes trivial corresponding to fully delocalized plane waves $\psi_n(x) \equiv \psi_{q_x}(x) = e^{iq_x x}$ and resulting in $E_{n,j} \equiv E_{q_x,j} = \tilde{E}_j + \hbar^2 q_x^2 / 2M$. Here, q_x is the component across the interface of the center-of-mass momentum $\mathbf{q} = (q_x, q_y)$. This implies that the center-of-mass motion of excitons is free and there is no quantization. For WSe₂-MoSe₂ LHs, we find CT excitons with an energy $E_{\text{CT}} \equiv E_{1,1s}$ that is approximately 88 meV lower than $E_{\text{Mo}} \equiv \tilde{E}_{1s}(x \gg 0)$ (and 178 meV lower than $E_{\text{W}} \equiv \tilde{E}_{1s}(x \ll 0)$). While spatially localized across the interface, CT excitons are delocalized along the junctions, where states with the momentum q_y along the interface form a one-dimensional parabolic dispersion. Overall, the wave-function of CT excitons reads $\Psi_{q_y}(\mathbf{r}, \mathbf{r})_r = \psi_{\text{CT}}(x) \phi_{1s}^x(\mathbf{r}) \frac{1}{\sqrt{L_y}} e^{iq_y y}$, where $\psi_{\text{CT}}(x) \equiv \psi_{1,1s}$ is the ground eigenstate in Eq. (1b) and L_y is the length of the sample along the interface.

2. SPATIOTEMPORAL EXCITON DYNAMICS

To investigate the spatiotemporal exciton dynamics in a lateral heterostructure, we first introduce a two-dimensional description of the dynamics and then exploit the sample symmetry to reduce it to the simpler one-dimensional case. For this purpose, we start with the Wigner functions $f_\alpha^{2D}(\mathbf{r}, \mathbf{q}, t) = \sum_{\mathbf{q}'} \langle \hat{X}_{\alpha, \mathbf{q}+\mathbf{q}'/2}^\dagger \hat{X}_{\alpha, \mathbf{q}-\mathbf{q}'/2} \rangle e^{i\mathbf{q}' \cdot \mathbf{r}}$ with $\alpha = \text{W, Mo}$ denoting WSe₂ and MoSe₂ excitons, respectively. Here, $\hat{X}_{\alpha, \mathbf{q}}^{(\dagger)}$ are the exciton annihilation (creation) operators [23, 24]. Using the Heisenberg equation of motion, we derive the spatiotemporal dynamics of the Wigner function yielding

$$\dot{f}_\alpha^{2D}(\mathbf{r}, \mathbf{q}, t) = -v_{\mathbf{q}} \cdot \nabla f_\alpha^{2D}(\mathbf{r}, \mathbf{q}, t) + \frac{f_\alpha^{2D, \circ}(\mathbf{r}, \mathbf{q}, t) - f_\alpha^{2D}(\mathbf{r}, \mathbf{q}, t)}{\tau_p} + f_\alpha^{2D, \text{d}}(\mathbf{r}, \mathbf{q}, t) + f_\alpha^{2D, \text{cap}}(\mathbf{r}, \mathbf{q}, t). \quad (2)$$

The first term describes the regular exciton propagation driven by the group velocity $v_{\mathbf{q}} = \hbar \mathbf{q} / M$ and the gradient in the occupation. The second term describes the phonon-driven thermalization toward the local Boltzmann distribution

$$f_\alpha^{2D, \circ}(\mathbf{r}, \mathbf{q}, t) = A \bar{f}_\alpha^{2D, \circ}(\mathbf{q}) n_\alpha(\mathbf{r}, t) \quad , \quad (3)$$

with $\bar{f}_\alpha^{2D, \circ}(\mathbf{q}) = \frac{2\pi \hbar^2}{M k_B T} \exp\left(-\frac{\hbar^2 |\mathbf{q}|^2}{2M k_B T}\right) / A$ being the normalized Boltzmann distribution, where $A = L_x L_y$ is the area of the sample. Here, $n_\alpha(\mathbf{r}, t) = \frac{1}{A} \sum_{\mathbf{q}} f_\alpha^{2D}(\mathbf{r}, \mathbf{q}, t)$ is the corresponding spatial exciton density. The phonon-driven thermalization is typically described by the Boltzmann collision term, which can be simplified in the relaxation-time approximation in the limit of $\sum_{\mathbf{q}'} \Gamma_{\alpha, \mathbf{q}; \alpha, \mathbf{q}'} (f_\alpha^{2D, \circ}(\mathbf{r}, \mathbf{q}', t) - f_\alpha^{2D}(\mathbf{r}, \mathbf{q}', t)) \approx 0$, where $\Gamma_{\alpha, \mathbf{q}; \alpha, \mathbf{q}'}$ are the scattering coefficients from exciton $|\alpha, \mathbf{q}'\rangle$ into $|\alpha, \mathbf{q}\rangle$ [25]. Such scattering coefficients provide the state-dependent scattering times $\tau_{\alpha, \mathbf{q}}^{-1} = \sum_{\mathbf{q}'} \Gamma_{\alpha, \mathbf{q}'; \alpha, \mathbf{q}}$ [25]. Here, we assume a state-independent $\tau_{\alpha, \mathbf{q}} = \tau_p$ with the microscopically obtained

phonon-driven scattering rate τ_p provided in Ref. [26].

While the first two terms in Eq. (2) are present also in regular TMD monolayers, the third and the fourth term are specific to lateral TMD heterostructures. The third term describes the drift of excitons driven by the energy offset at the interface and reads

$$f_{\alpha}^{2D,d}(\mathbf{r}, \mathbf{q}, t) = -\hbar^2 \int d\mathbf{q}' \mathcal{V}_{2D}(\mathbf{r}, \mathbf{q} - \mathbf{q}') f_{\alpha}^{2D}(\mathbf{r}, \mathbf{q}', t) = -\hbar \int d\mathbf{q}' \delta(q_y - q'_y) \mathcal{V}_{1D}(x, q - q') f_{\alpha}^{2D}(\mathbf{r}, \mathbf{q}', t). \quad (4)$$

Here, \mathcal{V} is induced by the excitonic energy offset and obtained by introducing the interface potential E_{α} (cf. Sec. 1) [27]. For the specific case, it reads

$$\mathcal{V}_{2D}(\mathbf{r}, \mathbf{q}'') = \frac{i}{(2\pi)^2 \hbar^3} \int d\mathbf{r}' \left[E_{\alpha} \left(\mathbf{r} + \frac{\mathbf{r}'}{2} \right) - E_{\alpha} \left(\mathbf{r} - \frac{\mathbf{r}'}{2} \right) \right] e^{-i\mathbf{q}'' \cdot \mathbf{r}'} = \frac{\delta(q''_y)}{\hbar} \mathcal{V}(x, q''_x), \quad (5a)$$

$$\text{with } \mathcal{V}_{1D}(x, q''_x) = \frac{i}{2\pi \hbar^2} \int_{-x_V}^{x_V} dx' \left[E_{\alpha} \left(x + \frac{x'}{2} \right) - E_{\alpha} \left(x - \frac{x'}{2} \right) \right] e^{-iq''_x x'} \quad , \quad (5b)$$

where we used the property of the LH interface potential to be invariant along the interface ($E_{\alpha}(\mathbf{r}) \equiv E_{\alpha}(x)$) and introduced a reasonable cutoff of $x_V = 25$ nm. Taylor expanding $E_{\alpha}(x \pm \frac{x'}{2})$ around x and after using $x'^m e^{-iq''_x x'} = (-1/i)^n \partial^n / \partial q''_x{}^n e^{-iq''_x x'}$ together with a partial integration, one can show that [25]

$$f_{\alpha}^{2D,d}(\mathbf{r}, \mathbf{q}, t) \approx \sum_n c_n \nabla_{\mathbf{r}}^n E_{\alpha}(\mathbf{r}) \cdot \nabla_{\mathbf{q}}^n f_{\alpha}^{2D}(\mathbf{r}, \mathbf{q}, t) \quad (6)$$

with complex constants c_n . For smooth-enough energies $E_{\alpha}(\mathbf{r})$, the first order of the expansion is enough, leading to the well-known semiclassical drift $\dot{f}_{\alpha}^{2D,d} = \nabla_{\mathbf{r}} E_{\alpha}(\mathbf{r}) \cdot \nabla_{\mathbf{q}} f_{\alpha}^{2D,d} / \hbar$. However, for realistic interface energies $E_{\alpha}(x)$ varying within a width $w = 2.4$ nm, all terms in Eq. (6) should be included.

Finally, the last term in Eq. (2) describes the trapping of MoSe₂ and WSe₂ excitons into the bound CT states. Similarly to the case of carrier-capture [28–30], this is expected to be driven by scattering with phonons and be local, i.e. taking place only when MoSe₂/WSe₂ excitons are located at the interface, where CT excitons are localized. In analogy to the intraband phonon-driven dynamics (second term in Eq. (2)), this is expressed in the relaxation time approximation as

$$\dot{f}_{\alpha}^{2D,\text{cap}} = \frac{\Delta n_{\alpha} f_{\alpha}^{2D,\circ} - f_{\alpha}^{2D}}{\tau_c}. \quad (7)$$

Here, we have introduced $\Delta n_{\alpha} = \frac{n_{\alpha}^{\circ}(\mathbf{r}, t)}{n_{\alpha}(\mathbf{r}, t)}$ as the ratio between the spatiotemporal exciton density $n_{\alpha}(\mathbf{r}, t)$ and its thermalized density $n_{\alpha}^{\circ}(\mathbf{r}, t)$. This is obtained after the introduction of CT excitons in the local thermalized spatial density of $\alpha = \text{Mo}, \text{W}$ excitons as $n_{\alpha}^{\circ}(\mathbf{r}, t) = d_{\alpha}(x) (n_{\alpha}(\mathbf{r}, t) + n_{\text{CT}}(\mathbf{r}, t))$ with

$$d_{\alpha}(x) = \left(1 + e^{-\frac{E_{\text{CT}} - E_{\alpha}(x)}{k_B T}} |\psi_{\text{CT}}(x)|^2 \sqrt{\frac{2\pi \hbar^2}{M k_B T}} \sum_{q_y} e^{-\frac{\hbar^2 q_y^2}{2M k_B T}} \right)^{-1}. \quad (8)$$

Since the capture is dominated by the emission of optical phonons, we assume $\tau_c = \tau_{\text{abs},c} e^{-\Omega/k_B T} / (1 + e^{-\Omega/k_B T})$, where $\tau_{\text{abs},c}$ is the temperature-dependent scattering time of MoSe₂ due to absorption of intravalley optical phonons with an energy of $\Omega = 30$ meV, which has been microscopically evaluated in Ref. [26]. Equation (7) implies a decrease of $n_{\alpha}(\mathbf{r}, t)$ as a consequence of trapping only when d_{α} differs from one. In agreement with the locality of carrier capture [28–30], this takes place only where the wavefunction $\psi_{\text{CT}}(x)$ of the bound CT exciton state is finite, hence close to the interface. Furthermore, the trapping is suppressed once the ratio between n_{α} and n_{CT} approaches the equilibrium value ($n_{\alpha} \approx n_{\alpha}^{\circ}$). This takes place when the CT exciton occupation is high enough to have a compensation between escape and trapping. As shown in the main manuscript, this compensation takes place on very different timescales depending on the temperature of the system.

Along the interface there is no energy offset, resulting in a drift-less diffusion [31, 32], while we expect a propagation across the interface driven by the energy offset. This can be described by a one-dimensional Wigner function $f_{\alpha}(x, q_x, t)$

obtained by integrating over space- and momentum along the interface yielding

$$f_\alpha(x, q, t) = \frac{1}{L_y} \sum_{q_y} \int dy f_\alpha^{2D}(\mathbf{r}_{CM}, \mathbf{q}_{CM}, t) \quad (9)$$

and for its temporal evolution

$$\dot{f}_\alpha(x, q_x, t) = \frac{1}{L_y} \sum_{q_y} \int dy \dot{f}_\alpha^{2D}(\mathbf{r}, \mathbf{q}, t) = -v_{q_x} \frac{\partial}{\partial x} f_\alpha + \frac{f_\alpha^\circ - f_\alpha}{\tau_p} + \dot{f}_\alpha^d + \dot{f}_\alpha^{\text{cap}} \quad (10a)$$

$$\text{with } \dot{f}_\alpha^d(x, q_x, t) = \sum_{q'_x} \mathcal{V}(x, q_x - q'_x) f_\alpha(x, q'_x, t) \quad \text{and} \quad \dot{f}_\alpha^{\text{cap}} = \frac{\Delta n_\alpha f_\alpha^\circ - f_\alpha}{\tau_c} . \quad (10b)$$

To obtain Eq. (10) we have assumed an identical distribution at the edges, i.e. $f_\alpha^{2D}((x, L_y/2), \mathbf{q}, t) \approx f_\alpha^{2D}((x, -L_y/2), \mathbf{q}, t)$ and introduced $f_\alpha^\circ(x, q, t) = \frac{1}{L_y} \sum_{q_y} \int dy f_\alpha^{2D\circ}(\mathbf{r}_{CM}, \mathbf{q}_{CM}, t)$ and $\mathcal{V}(x, q_x) = -2\pi\hbar/L_x \mathcal{V}_{1D}(x, q_x)$. The trapping of MoSe₂ and WSe₂ excitons forms CT excitons, whose spatial density $n_{CT}(x, t)$ has a profile across the interface determined by the wavefunction $\psi_{CT}(x)$, hence $n_{CT}(x, t) = |\psi_{CT}(x)|^2 N_{CT}(t)$, where $N_{CT}(t)$ is the time-dependent total population of CT excitons. As a consequence, Eq. (10) is coupled with the dynamics of the CT exciton density by

$$\dot{n}_{CT}(x, t) = |\psi_{CT}(x)|^2 \dot{N}_{CT}(t), \quad (11)$$

with the temporal evolution of $N_{CT}(t)$ following from the particle conservation as

$$\dot{N}_{CT}(t) = -\frac{1}{L_x} \sum_{q_x} \sum_{\alpha=\text{Mo,W}} \int dx \dot{f}_\alpha^{\text{cap}}(x, q_x, t). \quad (12)$$

3. PHOTOLUMINESCENCE

The optical excitation of TMD-based heterostructure leads to a coherent-to-incoherent population transfer [24, 33] followed by an energy-relaxation [24, 34, 35] potentially relevant also for transient transport phenomena [23, 36]. However, such transient effects last only few hundreds of femtoseconds at high temperatures [23], a timescale much shorter than the one investigated here. As a consequence, we start from an initial exciton distribution in the form of

$$f_\alpha^\circ(x, q_x, t=0) = L_x \bar{f}_\alpha^\circ(q_x) e^{-\frac{(x-x_L)^2}{2\Delta_0^2}} g_0(x) , \quad (13)$$

where $\bar{f}_\alpha^\circ(q_x) = 1/L_x \frac{\sqrt{2\pi\hbar}}{\sqrt{Mk_B T}} \exp\left[-\frac{\hbar^2 |q|^2}{2Mk_B T}\right]$ is the normalized Boltzmann distribution, while x_L and Δ_0 provide the position and the size of the laser spot, respectively. Finally, g_0 provides spatial inhomogeneities induced by the energy selection rule: in the case of an excitation resonant to WSe₂ we set $g_0(x) = \Theta(-x) + c_L \Theta(x)$, with $c_L = 0.01$ leading to a much larger excitation at the WSe₂ side ($x < 0$). In view of the 90 meV separation between the laser energy and E_{Mo} , the MoSe₂ excitons are formed less efficiently via phonon-driven non-resonant processes [37, 38]. In contrast, for the case of off-resonant excitations we expect only minor differences in the formation of WSe₂ and MoSe₂ excitons, leading to $g_0 = 1$.

The solution of Eq. (1) provides exciton wavefunctions, which allows to determine the oscillator strength γ_α . The latter is proportional to the probability $|\phi(\mathbf{r}=0)|^2 = \int dR_x |\psi(R_x)|^2 |\phi^{R_x}(\mathbf{r}=0)|^2$ of finding electrons and holes in the same position [1, 2]. In the specific case of the hBN-encapsulated WSe₂-MoSe₂ lateral heterostructure, the spatial separation of CT excitons leads to an oscillator strength that is about 35 times smaller than for MoSe₂ or WSe₂ excitons [2]. The spatial dipole furthermore leads to smaller binding energies in analogy to the case of interlayer excitons in vertical heterostructures [2, 39]. The energy-, space- and time-resolved photoluminescence $I(E, x, t)$ (PL) is determined by a product of the exciton density and the oscillator strength of the involved exciton species resulting in an Elliot formula [40, 41], which we have generalized to include CT excitons [2]

$$I(E, x, t) = \sum_\alpha \frac{f_\alpha^{2D,\circ}(x, \mathbf{q}=0, t) \tilde{\gamma}_\alpha (\tilde{\gamma}_\alpha + \Gamma)}{(E - E_\alpha)^2 + (\tilde{\gamma}_\alpha + \Gamma)^2}. \quad (14)$$

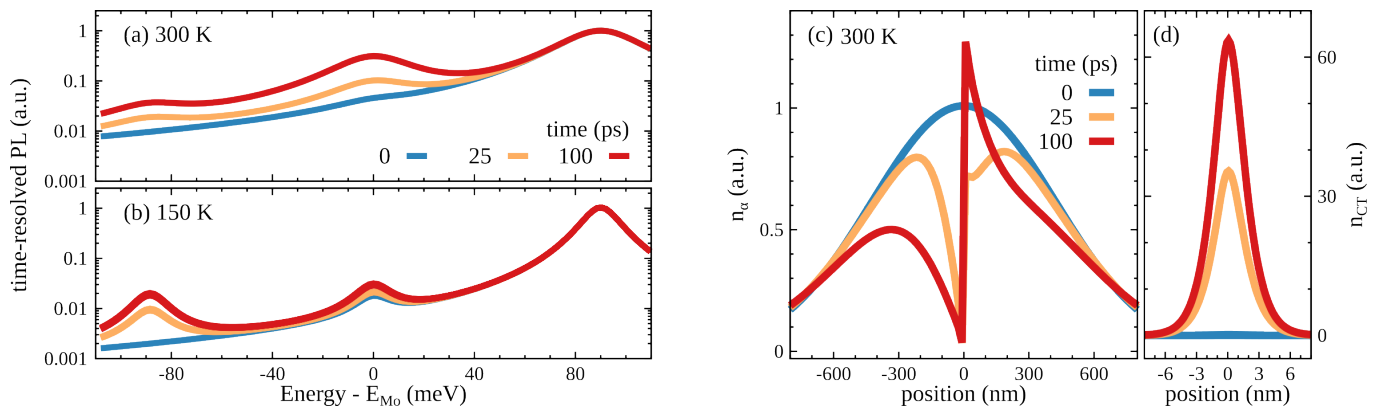


Fig. S2: (a-b) Energy- and time-resolved photoluminescence (PL) spectrum normalized to the X_W peak after micrometer excitation at the interface in resonance with X_W at (a) 300 K and (b) 150 K. At 300 K, the X_{M_0} resonance becomes comparable to X_W after approximately 100 ps reflecting the efficient exciton drift across the interface. Such a propagation is suppressed at the smaller temperature of 150 K, resulting in X_W remaining much larger than X_{M_0} . Furthermore, a small X_{CT} peak emitted from CT excitons appear after few hundreds of picoseconds. (c-d) Space-resolved densities of (a) WSe_2 and $MoSe_2$ excitons as well as of (b) CT excitons at 300 K after an off-resonant optical excitation at the interface. Similarly to the case of a resonant excitation (Fig. 2 of the main manuscript) we find the appearance of exciton depletion and accumulation at the WSe_2 and $MoSe_2$ side of the interface, respectively. At the same time, we observe the build-up of a large CT-exciton density that is about two orders of magnitude larger than the optically excited density.

The PL is influenced by the temperature-dependent exciton-phonon scattering rate $\Gamma = \hbar/2\tau_p$ and the radiative decay rate $\tilde{\gamma} = \gamma_\alpha |\psi_{\alpha, \mathbf{q}=0}|^2$, which is proportional to the $q = 0$ component of the squared wavefunction in center-of-mass momentum ψ_{q_x} . This is due to the conservation of momentum during the emission process [42]. Finally, for the case of the time-integrated PL, we consider an exciton lifetime $\tau = 175$ ps according to recent experiments in LHs [13].

In the main manuscript (Fig. 3(c)) we showed the time-resolved evolution of the energy- and time-resolved, space-integrated PL after resonant excitation at the interface at room temperature. In Fig. S2(b) we illustrate the PL at 150 K. For a direct comparison, in Fig. S2(a) we show again the results at 300 K, now taking cuts at given times. In this way, we clearly observe the delayed appearance of the X_{M_0} resonance, which is formed due to exciton propagation across the interface driven by the energy offset of the optically excited WSe_2 excitons. Thanks to this unidirectional propagation, the X_{M_0} resonance becomes as intense as X_W already after few hundreds of picoseconds. Furthermore, the time-resolved PL allows to resolve a small peak X_{CT} emitted by CT excitons. The situation becomes significantly different at 150 K, cf. Fig. S2(b). Here, the trapping into CT excitons becomes so efficient that only few optically excited WSe_2 excitons are able to cross the interface. As a consequence, the X_{M_0} resonance remains one order of magnitude smaller than the X_W peak even after 150 ps. The height of X_{M_0} increases only weakly compared to its initial value induced by the residual non-resonant excitation ($c_L = 0.01$ in Eq. 13). Furthermore, contrary to the room temperature case also the X_{CT} resonance becomes as intense as X_{M_0} . While the transport across the interface is suppressed by the decreasing temperature, the trapping still takes place, resulting in the formation of the X_{CT} resonance.

In the main manuscript, we have also considered a far-field excitation (laser spot of $1 \mu\text{m}$) resonant to the WSe_2 exciton energy. In Fig. S2(c-d), we show the same situation, but now after a high-energy excitation, resulting in an initial exciton density being spatially symmetric around the interface, cf. the cyan line in Fig. S2(c). Exploring the spatiotemporal exciton dynamics, we observe (i) an accumulation of exciton density at the $MoSe_2$ side and (ii) a depletion area at the WSe_2 side of the interface, cf. Fig. S2(c). This is induced by the unidirectional propagation driven by the energy offset between the two sides. Furthermore, we find the formation of (iii) a large CT exciton density, cf. Fig. S2(d). It becomes one (two) orders of magnitude larger than the initial exciton density after approximately 10 ps (100 ps).

[1] K. W. Lau, Calvin, Z. Gong, H. Yu, and W. Yao, Phys. Rev. B **98**, 115427 (2018), URL <https://link.aps.org/doi/10.1103/PhysRevB.98.115427>.

[2] R. Rosati, I. Paradisanos, L. Huang, Z. Gan, A. George, K. Watanabe, T. Taniguchi, L. Lombez, P. Renucci, A. Turchanin, et al., Nat. Commun. **14**, 2438 (2023), ISSN 2041-1723, URL <https://doi.org/10.1038/s41467-023-37889-9>.

- [3] X. Duan, C. Wang, J. C. Shaw, R. Cheng, Y. Chen, H. Li, X. Wu, Y. Tang, Q. Zhang, A. Pan, et al., *Nat. Nanotechnol.* **9**, 1024 (2014), ISSN 1748-3395, URL <https://doi.org/10.1038/nnano.2014.222>.
- [4] C. Huang, S. Wu, A. M. Sanchez, J. J. P. Peters, R. Beanland, J. S. Ross, P. Rivera, W. Yao, D. H. Cobden, and X. Xu, *Nat. Mater.* **13**, 1096 (2014), ISSN 1476-4660, URL <https://doi.org/10.1038/nmat4064>.
- [5] C. Zhang, M.-Y. Li, J. Tersoff, Y. Han, Y. Su, L.-J. Li, D. A. Muller, and C.-K. Shih, *Nat. Nanotech.* **13**, 152 (2018), ISSN 1748-3395, URL <https://doi.org/10.1038/s41565-017-0022-x>.
- [6] S. Xie, L. Tu, Y. Han, L. Huang, K. Kang, K. U. Lao, P. Poddar, C. Park, D. A. Muller, R. A. DiStasio, et al., *Science* **359**, 1131 (2018), URL <https://www.science.org/doi/abs/10.1126/science.aao5360>.
- [7] J. Kang, S. Tongay, J. Zhou, J. Li, and J. Wu, *Appl. Phys. Lett.* **102**, 012111 (2013), URL <https://doi.org/10.1063/1.4774090>.
- [8] Y.-H. Chu, L.-H. Wang, S.-Y. Lee, H.-J. Chen, P.-Y. Yang, C. J. Butler, L.-S. Lu, H. Yeh, W.-H. Chang, and M.-T. Lin, *Appl. Phys. Lett.* **113**, 241601 (2018), URL <https://doi.org/10.1063/1.5053144>.
- [9] P. K. Sahoo, S. Memaran, Y. Xin, L. Balicas, and H. R. Gutiérrez, *Nature* **553**, 63 (2018), ISSN 1476-4687, URL <https://doi.org/10.1038/nature25155>.
- [10] E. Najafidehaghani, Z. Gan, A. George, T. Lehnert, G. Q. Ngo, C. Neumann, T. Bucher, I. Staude, D. Kaiser, T. Vogl, et al., *Adv. Funct. Mater.* **31**, 2101086 (2021).
- [11] C. Herbig, C. Zhang, F. Mujid, S. Xie, Z. Pedramrazi, J. Park, and M. F. Crommie, *Nano Lett.* **21**, 2363 (2021), URL <https://doi.org/10.1021/acs.nanolett.0c04204>.
- [12] Y. Guo and J. Robertson, *Appl. Phys. Lett.* **108**, 233104 (2016).
- [13] D. Beret, I. Paradisanos, H. Lamsaadi, Z. Gan, E. Najafidehaghani, A. George, T. Lehnert, J. Biskupek, U. Kaiser, S. Shree, et al., *npj 2D Mater. Appl.* **6**, 84 (2022), ISSN 2397-7132, URL <https://doi.org/10.1038/s41699-022-00354-0>.
- [14] A. Pospischil, M. M. Furchi, and T. Mueller, *Nat. Nanotechnol.* **9**, 257 (2014), ISSN 1748-3395, URL <https://doi.org/10.1038/nnano.2014.14>.
- [15] B. W. H. Baugher, H. O. H. Churchill, Y. Yang, and P. Jarillo-Herrero, *Nat. Nanotechnol.* **9**, 262 (2014), ISSN 1748-3395, URL <https://doi.org/10.1038/nnano.2014.25>.
- [16] J. S. Ross, P. Klement, A. M. Jones, N. J. Ghimire, J. Yan, D. G. Mandrus, T. Taniguchi, K. Watanabe, K. Kitamura, W. Yao, et al., *Nat. Nanotechnol.* **9**, 268 (2014), ISSN 1748-3395, URL <https://doi.org/10.1038/nnano.2014.26>.
- [17] D. Thureja, A. Imamoglu, T. Smoleński, I. Amelio, A. Popert, T. Chervy, X. Lu, S. Liu, K. Barmak, K. Watanabe, et al., *Nature* **606**, 298 (2022), ISSN 1476-4687, URL <https://doi.org/10.1038/s41586-022-04634-z>.
- [18] M. Heithoff, . Moreno, I. Torre, M. S. G. Feuer, C. M. Purser, G. M. Andolina, G. Calajò, K. Watanabe, T. Taniguchi, D. M. Kara, et al., *ACS Nano* **18**, 30283 (2024), PMID: 39431410, URL <https://doi.org/10.1021/acsnano.4c04786>.
- [19] N. S. Rytova, *Proc. MSU, Phys., Astron.* **30**, 3 (1967).
- [20] L. Keldysh, *JETPL* **29**, 658 (1979).
- [21] S. Brem, J. Zipfel, M. Selig, A. Raja, L. Waldecker, J. D. Ziegler, T. Taniguchi, K. Watanabe, A. Chernikov, and E. Malic, *Nanoscale* **11**, 12381 (2019), URL <http://dx.doi.org/10.1039/C9NR04211C>.
- [22] A. Kormányos, G. Burkard, M. Gmitra, J. Fabian, V. Zólyomi, N. D. Drummond, and V. Fal'ko, *2D Mater.* **2**, 022001 (2015).
- [23] R. Rosati, R. Perea-Causín, S. Brem, and E. Malic, *Nanoscale* **12**, 356 (2020), URL <http://dx.doi.org/10.1039/C9NR07056G>.
- [24] S. Brem, M. Selig, G. Berghäuser, and E. Malic, *Sci. Rep.* **8**, 8238 (2018), ISSN 2045-2322, URL <https://doi.org/10.1038/s41598-018-25906-7>.
- [25] O. Hess and T. Kuhn, *Phys. Rev. A* **54**, 3347 (1996), URL <https://link.aps.org/doi/10.1103/PhysRevA.54.3347>.
- [26] M. Selig, G. Berghäuser, A. Raja, P. Nagler, C. Schüller, T. F. Heinz, T. Korn, A. Chernikov, E. Malic, and A. Knorr, *Nat. Commun.* **7**, 13279 (2016), ISSN 2041-1723, URL <https://doi.org/10.1038/ncomms13279>.
- [27] R. Rosati and F. Rossi, *Phys. Rev. B* **89**, 205415 (2014), URL <https://link.aps.org/doi/10.1103/PhysRevB.89.205415>.
- [28] M. Glanemann, V. M. Axt, and T. Kuhn, *Phys. Rev. B* **72**, 045354 (2005), URL <https://link.aps.org/doi/10.1103/PhysRevB.72.045354>.
- [29] D. Reiter, M. Glanemann, V. M. Axt, and T. Kuhn, *Phys. Rev. B* **75**, 205327 (2007), URL <https://link.aps.org/doi/10.1103/PhysRevB.75.205327>.
- [30] R. Rosati, D. E. Reiter, and T. Kuhn, *Phys. Rev. B* **95**, 165302 (2017), URL <https://link.aps.org/doi/10.1103/PhysRevB.95.165302>.
- [31] L. Yuan, B. Zheng, Q. Zhao, R. Kempt, T. Brumme, A. B. Kuc, C. Ma, S. Deng, A. Pan, and L. Huang, *ACS Nano* **17**, 15379 (2023), ISSN 1936-0851, URL <https://doi.org/10.1021/acsnano.2c12903>.
- [32] X. P. Vögele, D. Schuh, W. Wegscheider, J. P. Kotthaus, and A. W. Holleitner, *Phys. Rev. Lett.* **103**, 126402 (2009), URL <https://link.aps.org/doi/10.1103/PhysRevLett.103.126402>.
- [33] M. Selig, G. Berghäuser, M. Richter, R. Bratschitsch, A. Knorr, and E. Malic, *2D Mater.* **5**, 035017 (2018), URL <https://doi.org/10.1088/2F2053-1583%2Faabea3>.
- [34] R. Wallauer, R. Perea-Causin, L. Münster, S. Zajusch, S. Brem, J. Gädde, K. Tanimura, K.-Q. Lin, R. Huber, E. Malic, et al., *Nano Lett.* **21**, 5867 (2021), ISSN 1530-6984, URL <https://doi.org/10.1021/acs.nanolett.1c01839>.
- [35] D. Schmitt, J. P. Bange, W. Bennecke, A. AlMutairi, G. Meneghini, K. Watanabe, T. Taniguchi, D. Steil, D. R. Luke, R. T. Weitz, et al., *Nature* **608**, 499 (2022), ISSN 1476-4687, URL <https://doi.org/10.1038/s41586-022-04977-7>.
- [36] R. Rosati, K. Wagner, S. Brem, R. Perea-Causín, J. D. Ziegler, J. Zipfel, T. Taniguchi, K. Watanabe, A. Chernikov, and E. Malic, *Nanoscale* **13**, 19966 (2021), URL <http://dx.doi.org/10.1039/D1NR06230A>.
- [37] S. Shree, M. Semina, C. Robert, B. Han, T. Amand, A. Balocchi, M. Manca, E. Courtade, X. Marie, T. Taniguchi, et al.,

- Phys. Rev. B **98**, 035302 (2018), URL <https://link.aps.org/doi/10.1103/PhysRevB.98.035302>.
- [38] C. M. Chow, H. Yu, A. M. Jones, J. R. Schaibley, M. Koehler, D. G. Mandrus, R. Merlin, W. Yao, and X. Xu, npj 2D Mater. and App. **1**, 33 (2017), ISSN 2397-7132, URL <https://doi.org/10.1038/s41699-017-0035-1>.
- [39] S. Latini, K. T. Winther, T. Olsen, and K. S. Thygesen, Nano Lett. **17**, 938 (2017), ISSN 1530-6984.
- [40] S. W. Koch, M. Kira, G. Khitrova, and H. M. Gibbs, Nat. Mater. **5**, 523 (2006), ISSN 1476-4660, URL <https://doi.org/10.1038/nmat1658>.
- [41] S. Brem, A. Ekman, D. Christiansen, F. Katsch, M. Selig, C. Robert, X. Marie, B. Urbaszek, A. Knorr, and E. Malic, Nano Lett. **20**, 2849 (2020), ISSN 1530-6984.
- [42] M. Feierabend, Z. Khatibi, G. Berghäuser, and E. Malic, Phys. Rev. B **99**, 195454 (2019), URL <https://link.aps.org/doi/10.1103/PhysRevB.99.195454>.